PAPER

Cu superstructures hydrothermally reduced by leaves and derived Cu–Co₃O₄ hybrids for flexible solid-state electrochemical energy storage devices†

Huan Pang,[abc] Bing Li,[c] Qunxing Zhao,[b] Wen-Yong Lai[*b] and Wei Huang[*bd]

Cu–Co₃O₄ hybrids and activated carbon were employed to fabricate flexible solid-state electrochemical energy storage devices *via* facile processing. The resulting flexible devices showed a large specific capacitance of 530 mF cm⁻² with excellent mechanical flexibility, which offered a maximum volumetric energy density of 0.71 mW h cm⁻³, and delivered a maximum power density of 88.6 mW cm⁻³. What's more, the device showed an excellent cycling stability with only ∼5.2% decay after 6000 cycles.

1. Introduction

Energy storage is regarded as the most important problem facing humanity nowadays. Electrochemical batteries, fuel cells and electrochemical capacitors (ECs) are the main modern electrochemical energy storage devices.[1] According to charge storage mechanisms, supercapacitors (SCs) can be classified as (1) pseudocapacitors based on the redox charge storage mechanism, and (2) electric double layer capacitors (EDLCs) based on the electric double layer charge storage mechanism. SCs with a much higher power density are partly or completely replacing the common electrochemical batteries or fuel cells in many fields, thus attracting the attention of many countries (especially the developed countries) in developing SCs. From the viewpoint of practical application, SCs have been widely used in large industrial equipment, hybrid electric vehicles, renewable energy power plants, and memory back-up devices due to their qualities such as long life span, fast charge–discharge process, and rapid dynamics of charge propagation. Although SCs have many advantages compared to other electrochemical devices, they are also facing problems like lower energy density in the current technical stage, which will seriously impede their practical application.[2]

In the past years, electrochemical studies of cobalt based electrode materials were motivated since the chemical properties of cobalt are similar to those of nickel. In the 1990s, Conway and co-workers first reported research based on transition metal oxides for electrochemical energy storage.[3] Since then, studies on cobalt based materials, such as cobalt oxide,[4] cobalt hydroxide,[5] cobalt oxyhydroxides,[6] cobalt carbonates,[7] cobalt sulfide,[8] cobalt–nickel oxide/sulfide,[9,10] cobalt phosphate/phosphite[11,12] and cobalt compound related hetero-nanostructures/hybrids,[13–34] have flourished to a point where these materials with tunable properties have been prepared for various energy storage applications. For example, Fan *et al.* mainly focused on the studies on the fabrication of hetero-nanostructures or hybrids employed as electrochemical energy storage devices.[17–19]

In our previous work, we reported the facile synthesis of Cu superstructures by hydrothermal-reduction of natural leaves and the derived Cu–MnO₂ hybrids were used for fabricating high-performance SCs.[35] In this work, Cu–Co₃O₄ hybrids were synthesized and combined with activated carbon materials to fabricate flexible solid-state electrochemical energy storage (EES) devices, exhibiting a large specific capacitance (530 mF cm⁻²). Interestingly, the device possessed a maximum volumetric energy density of 0.71 mW h cm⁻³ at a current density of 2.0 mA cm⁻² and delivered a maximum power density of 88.6 mW cm⁻³ at a current density of 9.0 mA cm⁻². Remarkably, the device showed excellent mechanical flexibility with a bending angle of 0° up to 180°. What's more, the device demonstrated little capacitance change after over 6000 charge/discharge cycles at a current density of 9.0 mA cm⁻², and showed an excellent cycling stability with only ∼5.2% decay.

ᵃCollege of Chemistry and Chemical Engineering, Anyang Normal University, Anyang, Henan 455002, China

ᵇKey Laboratory for Organic Electronics & Information Displays (KLOEID), Institute of Advanced Materials (IAM), Jiangsu National Synergetic Innovation Center for Advanced Materials (SICAM), Nanjing University of Posts and Telecommunications (NUPT), Nanjing, Jiangsu 210023, China. E-mail: iamwylai@njupt.edu.cn

ᶜCollege of Chemistry and Chemical Engineering, Yangzhou University, Yangzhou, Jiangsu 225002, China

ᵈKey Laboratory of Flexible Electronics (KLOFE) and Institute of Advanced Materials (IAM), Jiangsu National Synergetic Innovation Center for Advanced Materials (SICAM), Nanjing Tech University (NanjingTech), 30 South Puzhu Road, Nanjing 211816, China. E-mail: wei-huang@njtech.edu.cn

† Electronic supplementary information (ESI) available. See DOI: 10.1039/c6ta00123h

2. Experimental

2.1 Materials preparation

Cu superstructures were hydrothermally reduced by using leaves as follows:[35] 0.20 g-$CuSO_4 \cdot 5H_2O$, 0.05 g-dry leaves (leaves were collected from a *Magnolia grandiflora* Linn tree and washed with distilled water and ethanol, and then dried in air), and 20 mL H_2O were mixed together. The above mixture was transferred into a Teflon-lined stainless steel autoclave, and held at 200 °C for 24 h. After the reaction, the obtained samples were easily separated from the remaining organic compounds because of their different densities. Finally, the as-prepared Cu was carefully washed with distilled water and ethanol, and dried in air.

Cu–Co_3O_4 hybrids were prepared as follows: 0.727 g $Co(NO_3)_2 \cdot 6H_2O$, 0.70 g $CO(NH_2)_2$, and 50 mL H_2O were mixed together, and the obtained pink solution was transferred into a Teflon-lined stainless steel autoclave with 0.1 g Cu superstructures dispersed into the above solution. The autoclave was heated at 95 °C for 8 h, and then cooled down to room temperature. The obtained sample was collected and rinsed with distilled water several times, followed by annealing at 350 °C in air gas for 3 h.

2.2 Electrochemical measurements

2.2.1 Fabrication of Cu superstructure–Co_3O_4 nanowire electrodes.
The working electrode was made from a mixture of active materials, acetylene black, and polytetrafluoroethylene (PTFE) with a weight ratio of 80 : 15 : 5, which was coated on a piece of nickel foam of about 1 cm^2, and pressed into a thin foil at a pressure of 5.0 MPa. The weight of the active sample is about 5 mg.

2.2.2 Electrochemical studies of all the electrodes in a three electrode system.
Electrochemical studies of Cu superstructure–Co_3O_4 nanowire electrodes were carried out on a CHI 660D electrochemical working station (Shanghai Chenhua Instrument, Inc.). All electrochemical measurements were carried out in a conventional three-electrode system equipped with a platinum electrode and a Hg/HgO electrode as counter and reference electrodes, respectively. Before the electrochemical measurement, we purged out O_2 from the solution by using the inert gas-Ar. The electrolyte was 3.0 M KOH solution. The capacitive properties of electrodes were determined by using cyclic voltammetry (CV) and galvanostatic charge–discharge techniques.

2.2.3 Fabrication of the flexible solid-state EESs.
The polyethylene terephthalate (PET) substrates were first covered with a layer of Pt film (~3 × 5 nm thick) and then coated with the slurry containing the active materials. The Cu–Co_3O_4 hybrids and activated carbon materials were prepared using a similar process to that used for the three electrode system and were used as the working electrode after drying. The specific capacitance of the Cu–Co_3O_4 hybrid electrode is 801 F g^{-1} at 1.0 A g^{-1} and that of the activated carbon is 215 F g^{-1} at 1.0 A g^{-1}. The ratio of the mass of the positive electrode to that of the negative electrode is 1 : 4,[26] which makes the same capacitance

of both the positive and negative electrodes. The poly-(vinylalcohol) (PVA)/KOH gel electrolyte was prepared as follows: the gel electrolyte (1.52 g PVA, 2.13 g KOH, and 15 mL H_2O) was prepared at 75 °C for 30 min and dropped onto the prepared sample to cover the active material after it was cooled naturally. Subsequently, two pieces of such electrodes were immersed in the PVA/KOH gel solution for 5–10 min to adsorb a layer of solid electrolyte. After the excess water was vaporized, two pieces of such electrodes containing the electrolyte were pressed together on a sheet out roller. In this way, the stacked all solid-state EESs were fabricated.

2.2.4 Electrochemical study of the flexible solid-state EESs.
CV measurements were carried out between 0 and 1.50 V on a PARSTAT 2273 electrochemical workstation. The flexible solid-state EESs were galvanostatically charged and discharged at current densities of 2.0–9.0 mA cm^{-2} in the voltage range of 0–1.50 V on an Arbin BT2000 electrochemical instrument. All the electrochemical measurements were conducted at room temperature.

2.3 Characterization

The morphology of the as-prepared samples was observed on a Hitachi S-4800 field-emission scanning electron microscope (FESEM) at an acceleration voltage of 10.0 kV. The phase analyses of the samples were performed by X-ray diffraction (XRD) on a Rigaku-Ultima III with Cu Kα radiation ($\lambda = 1.5418$ Å). Nitrogen adsorption–desorption measurements were performed on a Gemini VII 2390 Analyzer at 77 K using the volumetric method. The specific surface area was obtained from the N_2 adsorption–desorption isotherms and was calculated by the Brunauer–Emmett–Teller (BET) method. Transmission electron microscopy (TEM) images and high resolution TEM (HRTEM) images were captured on a JEM-2100 instrument microscope at an acceleration voltage of 200 kV.

3. Results and discussion

The crystallographic structure of the product was determined by X-ray powder diffraction (XRD). A typical XRD pattern of the product obtained by using sapless leaves from a *Magnolia*
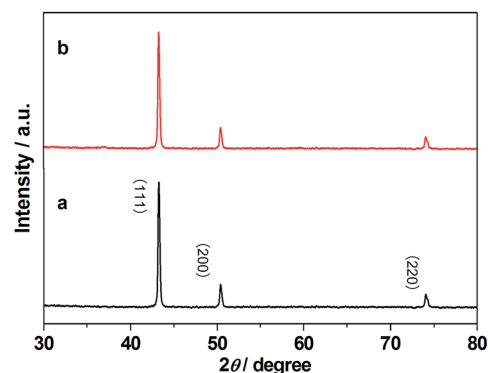

Fig. 1 XRD patterns of the as-prepared samples: (a) as-prepared Cu superstructures, and (b) Cu–Co_3O_4 hybrids.

This journal is © The Royal Society of Chemistry 2016

J. Mater. Chem. A, 2016, **4**, 4840–4847 | **4841**

grandiflora Linn tree as the reducing agent is shown in Fig. 1a. The strong diffraction peak is indexed to the cubic phase of Cu [Joint Committee for Powder Diffraction Studies File no. 04-0836]. The as-prepared Cu superstructures were reacted with cobalt nitrate hexahydrate under hydrothermal conditions (details can be seen in the Experimental section), and the hydrothermal product was calcined at 350° in air resulting in a black product. As shown in Fig. 1b, no noticeable peak of the Co_3O_4 phase is observed in the corresponding XRD pattern, indicating the small amount of Co_3O_4 coating.

The morphology of the as-prepared samples (Cu superstructures and Cu–Co_3O_4 hybrids) was characterized using FESEM and TEM. A panoramic view of the sample (Fig. 2a) shows that these Cu superstructures are ten micrometers in size with smooth surfaces interconnected by many polygon nanoplates. Moreover, the thickness of the as-prepared Cu superstructures is about 500 nm (Fig. 2b). As shown in Fig. 2c, the Cu superstructure–Co_3O_4 hybrid maintains the morphology of Cu superstructures while possessing a rough surface due to the Co_3O_4 nanowire coating as shown in Fig. 2d. The representative Co_3O_4 nanowires are clearly observed in Fig. 2e, manifesting the typical dimensions of 25–50 nm in length. The hybrid nature of the as-prepared Cu–Co_3O_4 superstructures can be further confirmed by using elemental mapping images in Fig. 2g–i, proving the generally uniform distribution of Cu, Co, and O elements within the superstructures. The atomic percent of all the elements present in the sample from the EDX analysis is $Cu_{100}Co_{1.5}O_2$, in which the mass content of Co is only 1.36%. TEM was further used to characterize the structure of Co_3O_4 nanowires (Fig. 2j), and the corresponding crystal lattice fringe spacing of 0.47 nm belongs to the (111) plane of the Co_3O_4

(JCPDS card: no. 43-1003) as shown in the inset of Fig. 2k. As demonstrated in a large magnification (Fig. 2k), the porous nanowire with a 2–4 nm pore size is composed of many Co_3O_4 nanocrystals. Consequently, the porous nature of the nanowire has provided sufficient surface/interface electroactive sites and facilitated the diffusion of ions/electrons, endowing the as-prepared Cu–Co_3O_4 hybrid with great potential in electrochemical capacitors.

The specific surface areas and porosity of the as-synthesized Cu–Co_3O_4 hybrids were analysed by N_2 adsorption–desorption measurements. As shown in Fig. 3a, the N_2 adsorption–desorption isotherms can be ascribed to type IV, suggesting the presence of mesopores in the Cu–Co_3O_4 hybrids, and the specific surface area of the Cu–Co_3O_4 hybrids is 45.7 m^2 g^{-1}, which is larger than that of the Cu superstructure (25.7 m^2 g^{-1}). The average pore size of the Cu–Co_3O_4 hybrids is 2–4 nm in Fig. 3b, which is consistent with the HRTEM results in Fig. 2k.

The electrochemical properties of the as-prepared Cu–Co_3O_4 hybrids were investigated using CV and galvanostatic charge–discharge measurements. Fig. 4a shows the CV curves of the electrode at different scan rates from 5.0 to 50 mV s^{-1} within the potential window of 0.0 to 0.48 V in 3.0 M KOH solution. The shape of these CV curves is different from the electric double-layer capacitance. Each CV curve consists of a pair of large redox peaks, owing to the reaction of Co^{2+} to Co^{3+} occurring at the surface of the Cu–Co_3O_4 hybrid electrode. Interestingly, the redox current increases with the scan rate. Furthermore, it was found that the oxidation and reduction peaks shift toward higher and lower potential with a large potential separation, which was mainly attributed to the resistance of the electrode. Fig. 3b presents the charge–discharge curves of the Cu–Co_3O_4
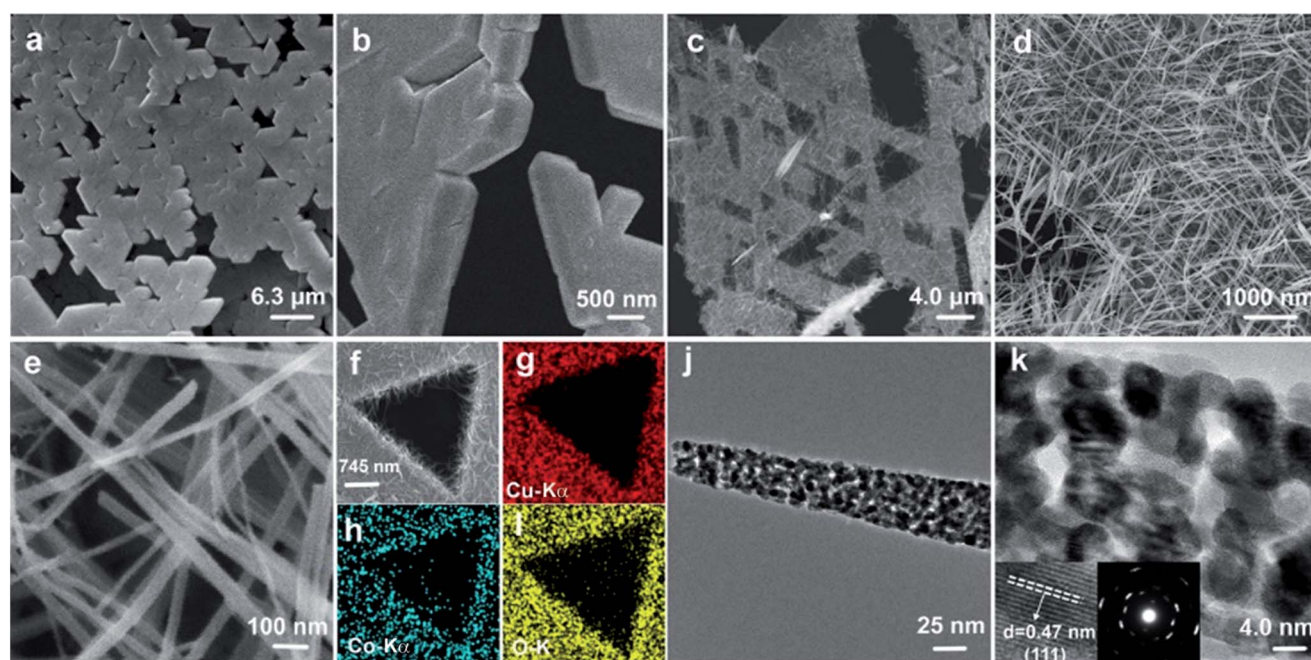

Fig. 2 (a and b) SEM images of the as-prepared Cu superstructures; (c–f) SEM images of the Cu–Co_3O_4 hybrids; (g–i) EDS-mapping images of different elements; (j and k) TEM images. Left inset of k – the crystal lattice space, and the right inset of k – the corresponding SAED patterns.
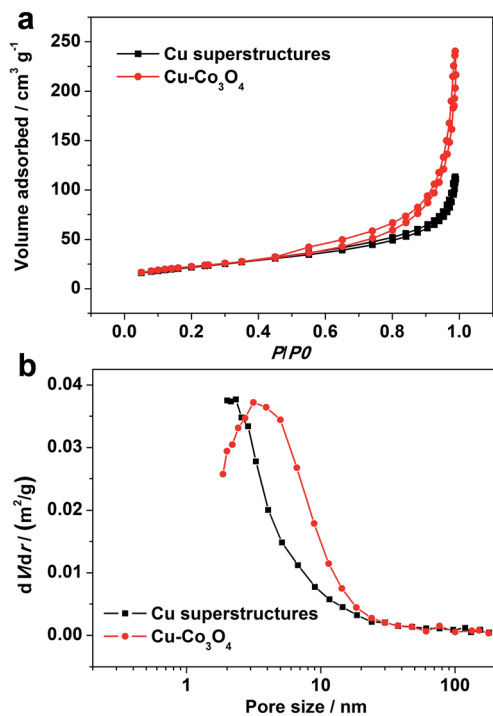
4842 | *J. Mater. Chem. A*, 2016, **4**, 4840–4847

This journal is © The Royal Society of Chemistry 2016

Fig. 3 (a) N$_2$ adsorption–desorption isotherm curves of the as-prepared samples and (b) the corresponding pore size distribution curves.

hybrid electrode at different current densities of 0.5 to 5.0 A g^{-1}. The shapes of the charge–discharge curves mainly are not characteristic of the double-layer capacitance in Fig. 4b, which is in agreement with the CV tests. The specific capacitance of the

the electrodes was calculated from the discharge curves according to the following equation [eqn (1)]:

$$C = (I\Delta t)/(m\Delta V) \tag{1}$$

in which I, Δt, m, and ΔV are the discharge current [A], the time for discharge [s], the weight of the active materials [g] in the electrodes, and the voltage interval of the discharge [V], respectively. A specific capacitance of 908 F g^{-1} was obtained at a current density of 0.5 A g^{-1}. When the current density increased to 5.0 A g^{-1}, the specific capacitance still remained 467 F g^{-1} as shown in Fig. 4c. The cycling performance of the Cu–Co$_3$O$_4$ hybrid electrode at 3.0 A g^{-1} for 6000 cycles is shown in Fig. 4d, and it is seen that the specific capacitance is 583 F g^{-1} even after 6000 cycles. The stable specific capacitance can be attributed to the large accessible surface area and porous structure, providing effective diffusion channels for the electrolyte ions, thus improving the diffusion of ions and the electrolyte. Furthermore, we have also prepared Co$_3$O$_4$ particles for comparison (detailed information can be seen in Fig. S1 and S2†). It is seen that the morphology of the as-prepared Co$_3$O$_4$ particle is formless particles with sizes of 200–1500 nm in Fig. S1.† The specific capacitance of the as-prepared Co$_3$O$_4$ particle electrode is only 290 F g^{-1} at 0.5 A g^{-1} in Fig. S2c.† After 6000 cycles, the specific capacitance of the as-prepared Co$_3$O$_4$ particle electrode is only 35 F g^{-1} in Fig. S2d.† The electrochemical impedance spectra of the as-prepared Cu–Co$_3$O$_4$ hybrid and Co$_3$O$_4$ particle electrode at room temperature are shown in Fig. S3.† Due to the good conductivity of the inner Cu superstructure, the Cu–Co$_3$O$_4$ hybrid electrode shows better conductivity than the pure Co$_3$O$_4$ particle electrode, which can improve the electrochemical capacitor performance.
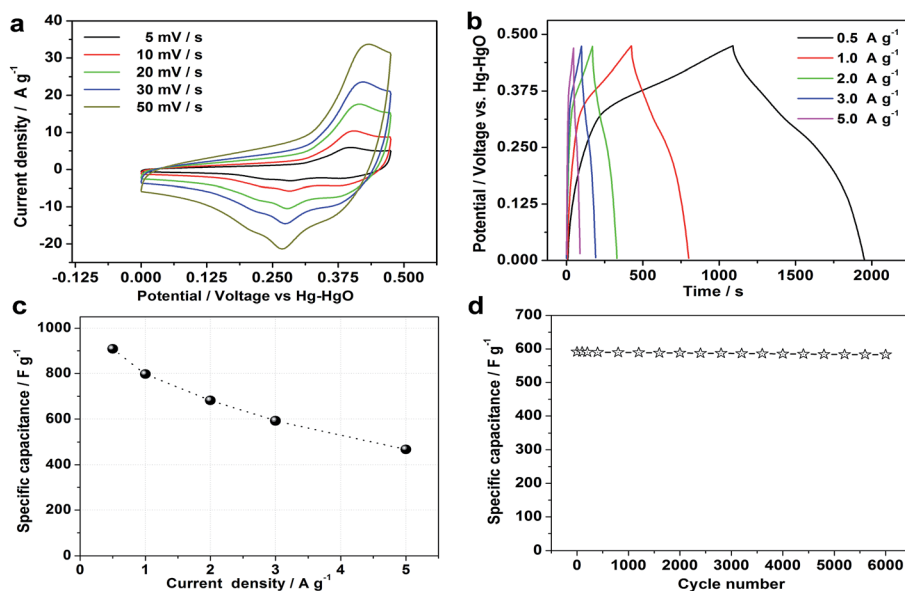

Fig. 4 (a) Cyclic voltammetry experiments within the 0.0–0.48 V range at a scan rate of 5–50 mV s^{-1} were performed on the Cu–Co$_3$O$_4$ hybrid electrodes in a 3.0 M KOH solution at room temperature; (b) the galvanostatic charge–discharge curves of the Cu–Co$_3$O$_4$ hybrid electrode at current densities of 0.5–5.0 A g^{-1} in a 3.0 M KOH solution; (c) specific capacitances of Cu–Co$_3$O$_4$ hybrid electrodes derived from the discharging curves at a current density of 0.5–5.0 A g^{-1} in a 3.0 M KOH solution; (d) cycling performance of the Cu–Co$_3$O$_4$ hybrid electrode at 3.0 A g^{-1} for 6000 cycles.

This journal is © The Royal Society of Chemistry 2016

J. Mater. Chem. A, 2016, **4**, 4840–4847 | **4843**

To develop flexible power sources, flexible solid-state EESs ($Cu–Co_3O_4$ hybrids//activated carbons) were then fabricated based on the $Cu–Co_3O_4$ hybrids and activated carbon as active electrode materials with the aid of our previous method (see details in the Experimental section). Fig. 5a shows a series of CV measurements of the $Cu–Co_3O_4$ hybrid//activated carbon EESs with different cell voltages varying from 0.0–1.0 V to 0.0–1.5 V. At 1.0 V, the presence of redox peaks (in the region between 0.0 and 1.0 V) indicates that the electrochemical energy storage properties of the cell originate from the positive electrode (the $Cu–Co_3O_4$ hybrids). The surrounding area from the corresponding CV curve is the largest when the operating potential is increased to 1.5 V, denoting the potential at which most faradic reactions will occur. More importantly, the charge–discharge curves of the flexible solid-state EES at a current density of 3.0 mA cm^{-2} are nearly symmetric at an operating potential of 1.5 V (Fig. 5b). These ideal capacitive characteristics with a rapid $I–U$ response are probably attributed to the small equivalent series resistance of the device.[36] Fig. 5c shows the specific capacitances of the flexible solid-state EES device calculated based on the discharge curves in Fig. 5b. The specific capacitance increases from 35 to 484 mF cm^{-2} with increasing the operating potential from 1.0 to 1.5 V. According to the equation $E = CU^2/2$, the amount of the stored energy and delivered power of the flexible solid-state EES device (the potential window is 0–1.5 V) can be enhanced by at least 2.25-fold compared with those with the potential window of 0–1.0 V. As a result of the increased faradaic reactions and the large voltage window, considerably improved energy density and powder density can be obtained.

CV curves of the flexible solid-state EES device (5, 10, and 50 mV s^{-1}) were also measured as shown in Fig. 6a (the potential window is 0.0–1.5 V). According to the shape of the CV curves, a good electrochemical energy storage capacity is observed at all scan rates. Interestingly, the shape of the CV curve can still be well maintained even at a scan rate of 50 mV s^{-1}, indicating the good rate capability of the flexible solid-state EES device. The galvanostatic charge–discharge curves of the flexible solid-state EES device at different current densities are shown in Fig. 6b, and the specific capacitance reached 530 mF cm^{-2} at a current density of 2.0 mA cm^{-2}. Derived from the data in Fig. 6b, other specific capacitances are plotted in Fig. 6c, in which the flexible solid-state EES device exhibited good rate capability (62.2% retention at even 9.0 mA cm^{-2}).

Interestingly, the stable cycling performance of the flexible solid-state EES device was also maintained at each current density, which further confirmed its good rate stability. 6000 charge–discharge cycling tests were carried out to examine the long-term cycle ability of the flexible solid-state EES device (Fig. 6d). During the cycling process at a current density of 9.0 mA cm^{-2}, only a small decay of the capacitance was observed. In addition, the decay could be ascribed to the consumption of the gel electrolyte, originating from an irreversible reaction from active materials and electrolytes.[37] After 6000 cycles, the specific capacitance of the flexible solid-state EES device was still approximately 94.8% of its initial capacitance (330 mF cm^{-2}), which strongly verified the good cycling performance of the flexible solid-state EES device. The morphology of materials affects the electrochemical activity. The SEM images of the $Cu–Co_3O_4$ hybrid from the EES device recorded at 9.0 mA cm^{-2} for 6000 cycles are shown in Fig. S4.† The outline of the superstructure was observed; however the Co_3O_4 nanorods disappeared and thus caused decay of the capacitance.
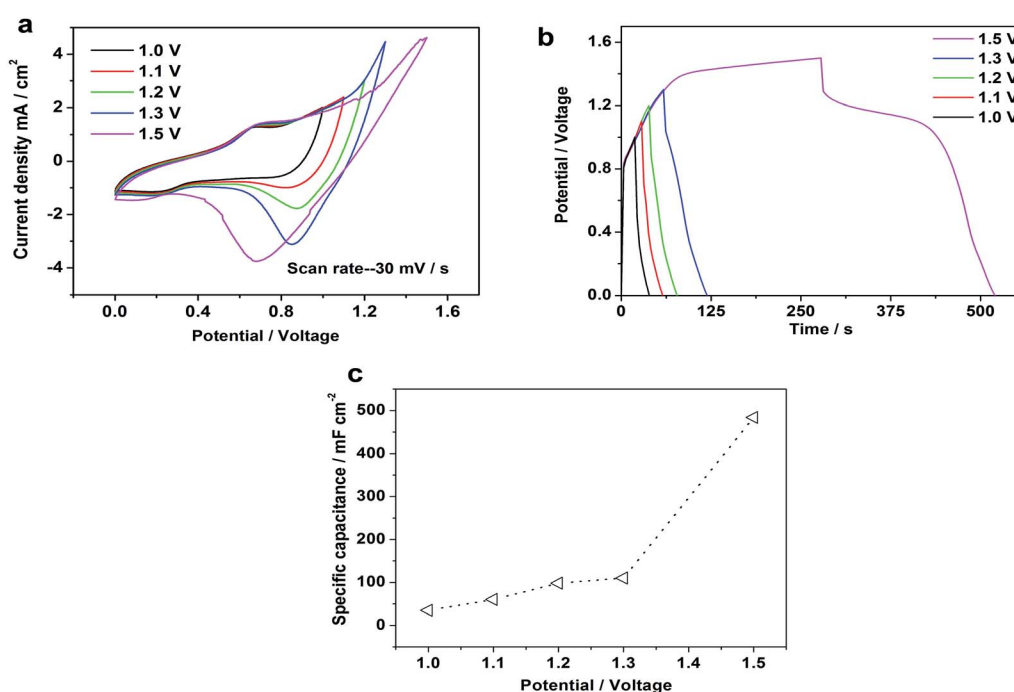

Fig. 5 (a) CV curves; (b) galvanostatic charge–discharge curves and (c) specific capacitance curves of the flexible solid-state EES ($Cu–Co_3O_4$ hybrids//activated carbons) with the increase of the potential.

4844 | J. Mater. Chem. A, 2016, 4, 4840–4847

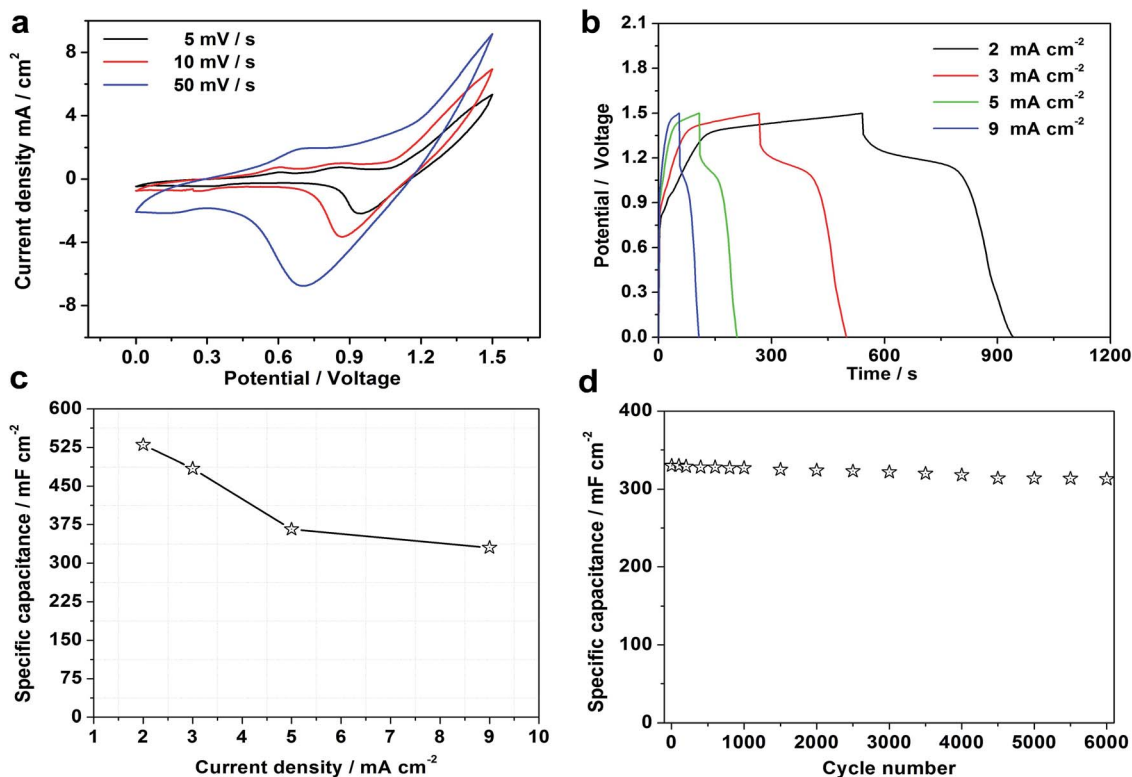This journal is © The Royal Society of Chemistry 2016

Fig. 6 (a) CV curves with scan rates between 5 and 50 mV s^{-1}; (b) galvanostatic charge–discharge curves at current densities ranging from 2.0 to 9.0 mA cm^{-2} of the device in the potential window of 0.0–1.5 V; (c) the specific capacitance was calculated based on the data in (b); (d) cycling performance of the device at 9.0 mA cm^{-2} for 6000 cycles.

In order to test the flexibility of our solid-state EES, electrochemical tests were conducted with different bending angles (Fig. 7) at a scan rate of 30 mV s^{-1}. As shown in Fig. 7, the CV curves with different bending angles only differed slightly. It is worthwhile to mention that the specific capacitance of the device was maintained throughout the bending process.

The energy and power densities of the flexible solid-state EES device measured at different scan rates are shown in Fig. 8. A maximum volumetric energy density of 0.71 mW h cm^{-3} was achieved under an operating potential of 1.5 V. Additionally, the maximum power density of the flexible solid-state EES was 86.6 mW cm^{-3} at 9.0 mA cm^{-2}. These values of the as-assembled flexible solid-state EES device are comparable to those of the state-of-the-art devices reported recently as shown in Fig. 8.[38–48]
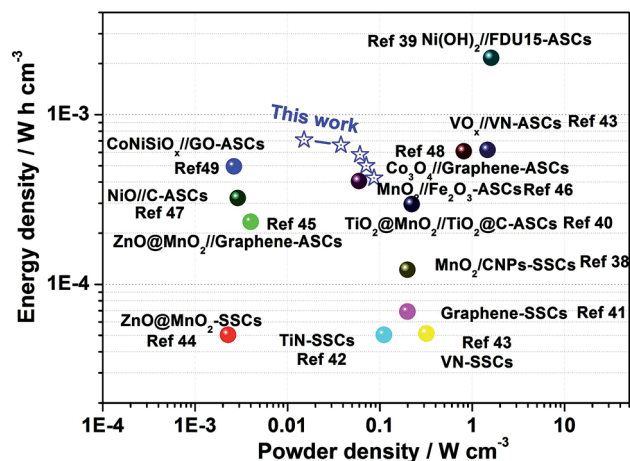

Fig. 7 Cyclic voltammetry within a 0–1.5 V range at a scan rate of 30 mV s^{-1} with four bending modes (inset).

Fig. 8 Ragone plots of the as-prepared device. The values reported for other previous devices are added for comparison.[38–49]

This journal is © The Royal Society of Chemistry 2016

J. Mater. Chem. A, 2016, **4**, 4840–4847 | **4845**

The maximum energy density of our flexible solid-state EES device is larger than that of most devices in Fig. 8, but is smaller than that of $Ni(OH)_2$//FDU15 (2.16 mW h cm^{-3}).[45] Additionally, the flexible solid-state EES device exhibited much higher maximum power density than the recently reported devices: $ZnO@MnO_2$,[44] $ZnO@MnO_2$//graphene,[45] MnO_2//Fe_2O_3,[46] NiO//C,[47] and $CoNiSiO_x$//GO,[49] while possessing lower performance than other devices in Fig. 8. Bearing all these results in mind, we can draw the conclusion that the $Cu–Co_3O_4$ hybrid is very promising as a high energy-density anode material for flexible solid state EES devices. It is noted that the improved performance can be attributed to the effect of high ion permeability of the porous structure and the abundant electron pathways within the inner Cu superstructures.

4. Conclusions

In summary, $Cu–Co_3O_4$ hybrids were successfully prepared from Cu superstructures hydrothermally reduced by leaves and $Co(NO_3)_2$. Flexible solid-state EES devices based on the $Cu–Co_3O_4$ hybrid//activated carbon have demonstrated great performance, representing the first report of this material being applied for SCs. The flexible solid-state device showed little capacitance change after over 6000 charge/discharge cycles at a current density of 9.0 mA cm^{-2}, and exhibited an excellent cycling stability with only ~5.2% decay. Notably, the device shows excellent mechanical flexibility for bending angles between 0° and 180°. Because of the simplicity of synthesis and device fabrication processes, and the eco-friendly nature of the materials, this flexible solid-state EES holds great promise for integration into various flexible electronic systems such as power-on-chip systems, roll-up display panels and solar energy harvesters.

Acknowledgements

Notes and references

1 X. Dong, Z. Guo, Y. Song, M. Hou, J. Wang, Y. Wang and Y. Xia, *Adv. Funct. Mater.*, 2014, **24**, 3405.
2 C. Z. Wu, F. Feng and Y. Xie, *Chem. Soc. Rev.*, 2013, **42**, 5157.
3 B. E. Conway, *J. Electrochem. Soc.*, 1991, **138**, 1539.
4 V. Srinivasan and J. W. Weidner, *J. Electrochem. Soc.*, 1997, **144**, L210.
5 C. Lin, J. A. Ritter and B. N. Popov, *J. Electrochem. Soc.*, 1998, **145**, 4097.
6 C.-H. Chen, S. F. Abbas, A. Morey, S. Sithambaram, L.-P. Xu, H. F. Garces, W. A. Hines and S. L. Suib, *Adv. Mater.*, 2008, **20**, 1205.
7 L. Hu, Q. Peng and Y. Li, *J. Am. Chem. Soc.*, 2008, **130**, 16136.
8 F. Tao, Y. Q. Zhao, G. Q. Zhang and H. L. Li, *Electrochem. Commun.*, 2007, **9**, 1282.
9 X. Lu, X. Huang, S. Xie, T. Zhai, C. Wang, P. Zhang, M. Yu, W. Li, C. Liang and Y. Tong, *J. Mater. Chem.*, 2012, **22**, 13357.
10 L. Yu, L. Zhang, H. B. Wu and X. W. Lou, *Angew. Chem.*, 2014, **126**, 3785.
11 H. Pang, Z. Yan, W. Wang, J. Chen, J. Zhang and H. Zheng, *Nanoscale*, 2012, **4**, 5946.
12 H. Pang, Y. Liu, J. Li, Y. Ma, G. Li, Y. Ai, J. Chen, J. Zhang and H. Zheng, *Nanoscale*, 2013, **5**, 503.
13 C. Shang, S. Dong, S. Wang, D. Xiao, P. Han, X. Wang, L. Gu and G. Cui, *ACS Nano*, 2013, **7**, 5430.
14 F. Yang, J. Yao, F. Liu, H. He, M. Zhou, P. Xiao and Y. Zhang, *J. Mater. Chem. A*, 2013, **1**, 594.
15 X. Wang, A. Sumboja, M. Lin, J. Yan and P. S. Lee, *Nanoscale*, 2012, **4**, 7266.
16 D. T. Dam, X. Wang and J.-M. Lee, *RSC Adv.*, 2012, **2**, 10512.
17 J. Liu, J. Jiang, C. Cheng, H. Li, J. Zhang, H. Gong and H. J. Fan, *Adv. Mater.*, 2011, **23**, 2076.
18 C. Guan, J. Liu, C. Cheng, H. Li, X. Li, W. Zhou, H. Zhang and H. J. Fan, *Energy Environ. Sci.*, 2011, **4**, 4496.
19 X. Xia, J. Tu, Y. Zhang, X. Wang, C. Gu, X.-B. Zhao and H. J. Fan, *ACS Nano*, 2012, **6**, 5531.
20 L.-Q. Mai, F. Yang, Y.-L. Zhao, X. Xu, L. Xu and Y.-Z. Luo, *Nat. Commun.*, 2011, **2**, 381.
21 H. Zhang, Y. Chen, W. Wang, G. Zhang, M. Zhuo, H. Zhang, T. Yang, Q. Li and T. Wang, *J. Mater. Chem. A*, 2013, **1**, 8593.
22 K. Xu, R. Zou, W. Li, Y. Xue, G. Song, Q. Liu, X. Liu and J. Hu, *J. Mater. Chem. A*, 2013, **1**, 9107.
23 J. Han, Y. Dou, J. Zhao, M. Wei, D. G. Evans and X. Duan, *Small*, 2013, **9**, 98.
24 C. Zhou, Y. Zhang, Y. Li and J. Liu, *Nano Lett.*, 2013, **13**, 2078.
25 L. Han, P. Tang and L. Zhang, *Nano Energy*, 2014, **7**, 42.
26 H. B. Li, M. H. Yu, F. X. Wang, P. Liu, Y. Liang, J. Xiao, C. X. Wang, Y. X. Tong and G. W. Yang, *Nat. Commun.*, 2013, **4**, 1894.
27 B. Wang, T. Zhu, H. B. Wu, R. Xu, J. S. Chen and X. W. (David) Lou, *Nanoscale*, 2012, **4**, 2145.
28 T. Zhu, J. S. Chen and X. W. Lou, *J. Mater. Chem.*, 2010, **20**, 7015.
29 Y. C. Wang, T. Zhou, K. Jiang, P. M. Da, Z. Peng, J. Tang, B. Kong, W.-B. Cai, Z. Q. Yang and G. F. Zheng, *Adv. Energy Mater*, 2014, **4**, 1400696.

30 J. P. Liu, J. Jiang, C. Cheng, H. X. Li, J. X. Zhang, H. Gong and H. J. Fan, *Adv. Mater.*, 2011, **23**, 2076.

31 X. H. Cao, B. Zheng, X. H. Rui, W. H. Shi, Q. Y. Yan and H. Zhang, *Angew. Chem., Int. Ed.*, 2014, **53**, 1404.

32 X. H. Cao, B. Zheng, W. H. Shi, J. Yang, Z. X. Fan, Z. M. Luo, X. H. Rui, B. Chen, Q. Y. Yan and H. Zhang, *Adv. Mater.*, 2015, **27**, 4695.

33 G. Z. Sun, X. Zhang, R. Z. Lin, J. Yang, H. Zhang and P. Chen, *Angew. Chem., Int. Ed.*, 2015, **54**, 4651.

34 T. Brousse, D. Belanger and J. W. Long, *J. Electrochem. Soc.*, 2015, **162**, A5185.

35 H. Pang, S. Wang, G. Li, Y. Ma, J. Li, X. Li, L. Zhang, J. Zhang and H. Zheng, *J. Mater. Chem. A*, 2013, **1**, 5053.

36 L.-F. Chen, Z.-H. Huang, H.-W. Liang, Q.-F. Guan and S.-H. Yu, *Adv. Mater.*, 2013, **25**, 4746.

37 X. F. Wang, B. Liu, R. Liu, Q. F. Wang, X. J. Hou, D. Chen, R. M. Wang and G. Z. Shen, *Angew. Chem., Int. Ed.*, 2014, **53**, 1849.

38 Z. B. Lei, J. T. Zhang and X. S. Zhao, *J. Mater. Chem.*, 2012, **22**, 153.

39 X. L. Dong, Z. Y. Guo, Y. F. Song, M. Y. Hou, J. Q. Wang, Y. G. Wang and Y. Y. Xia, *Adv. Funct. Mater.*, 2014, **24**, 3405.

40 X. H. Lu, M. H. Yu, G. M. Wang, T. Zhai, S. L. Xie, Y. C. Ling, Y. X. Tong and Y. Li, *Adv. Mater.*, 2013, **25**, 267.

41 M. F. El-Kady, V. Strong, S. Dubin and R. B. Kaner, *Science*, 2012, **335**, 1326.

42 X. H. Lu, G. M. Wang, T. Zhai, M. H. Yu, S. L. Xie, Y. C. Ling, C. L. Liang, Y. X. Tong and Y. Li, *Nano Lett.*, 2012, **12**, 5376.

43 X. H. Lu, M. H. Yu, T. Zhai, G. M. Wang, S. L. Xie, T. Y. Liu, C. L. Liang, Y. X. Tong and Y. Li, *Nano Lett.*, 2013, **13**, 2628.

44 P. H. Yang, X. Xiao, Y. Z. Li, Y. Ding, P. F. Qiang, X. H. Tan, W. J. Mai, Z. Y. Lin, W. Z. Wu, T. Q. Li, H. Y. Jin, P. Y. Liu, J. Zhou, C. P. Wong and Z. L. Wang, *ACS Nano*, 2013, **7**, 2617.

45 Z. L. Wang, Z. Zhu, J. Qiu and S. Yang, *J. Mater. Chem. C*, 2014, **2**, 1331.

46 X. H. Lu, Y. X. Zeng, M. H. Yu, T. Zhai, C. L. Liang, S. L. Xie, M. S. Balogun and Y. X. Tong, *Adv. Mater.*, 2014, **26**, 3148.

47 Y. Qian, R. Liu, Q. Wang, J. Xu, D. Chen and G. Shen, *J. Mater. Chem. A*, 2014, **2**, 10917.

48 X. Wang, B. Liu, R. Liu, Q. Wang, X. Hou, D. Chen, R. Wang and G. Shen, *Angew. Chem., Int. Ed.*, 2014, **126**, 1880.

49 J. Zhao, M. Zheng, Z. Run, J. Xia, M. Sun and H. Pang, *J. Power Sources*, 2015, **285**, 386.